

High-throughput Density Measurement Using Magnetic Levitation

Supplemental Information

Shencheng Ge¹, Yunzhe Wang¹, Nico Deshler¹, Daniel J. Preston¹, and George M.

Whitesides^{1,2,3*}

¹ Department of Chemistry & Chemical Biology, Harvard University, 12 Oxford Street,
Cambridge, MA 02138, USA

² Wyss Institute for Biologically Inspired Engineering, Harvard University, 60 Oxford
Street, Cambridge, MA 02138, USA

³ Kavli Institute for Bionano Science & Technology, Harvard University, 29 Oxford
Street Cambridge, MA 02138, USA

*Corresponding author: gwhitesides@gmwgroup.harvard.edu

Materials

Blood samples were purchased from Blood Research Components, LLC.

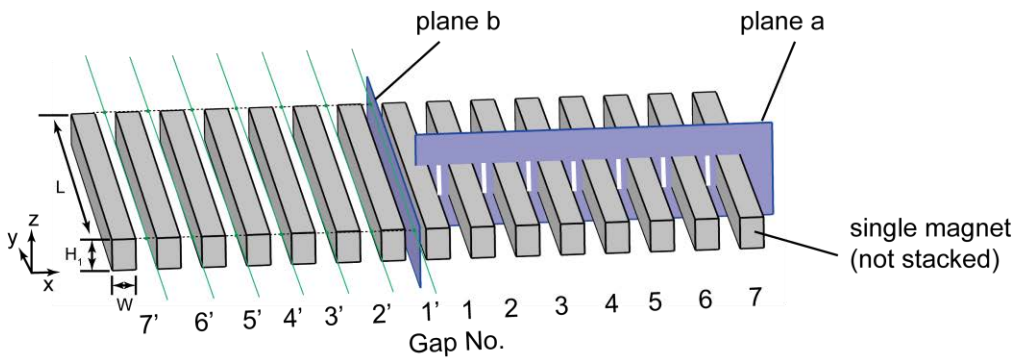
Selecting the number and dimensions of magnets

Simulation in COMSOL shows that a minimum number of 15 magnets and a minimum length of ~ 101.6 mm (four inches) of the magnets are required to create a nearly uniform magnetic field in all 12 gaps to accommodate all 12 columns of tubes on a 96-well plate. We used an array of 15 magnets of 101.6 mm \times 4.8 mm \times 6.4 mm (L \times W \times H)—half of the final magnet array we used in this study—as an example to illustrate the design.

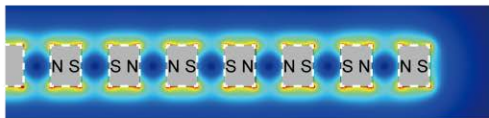
First, we found that the profile of the magnetic field in the outermost gaps deviates slightly from those in the middle, which are virtually indistinguishable. For example, the strength of the field along y-axis (along the longest dimension of the magnets) at both $z=H_1/2$ and $z=H_1$ (Figure S1A, plane b, green lines. H_1 is the height of the magnet, and $z=0$ is defined at its bottom face) in the middle of the outermost gaps 7 and 7' deviates from those in other gaps (Figures S1C and S1E). Similarly, the z-component of the magnetic field along the vertical centerlines of the gaps (Figure S1A, white lines on plane a) in the outermost gaps deviates from those in other gaps (Figures S1B and S1D). While the outermost gaps are similarly functional to levitate objects, we simply excluded them in this study for simplicity (e.g., to avoid having to carry out separate calibrations for density measurements).

Second, we found that a minimum length of 101.6 mm (four inches) of a magnet is required to create a uniform profile of the magnetic field in the gaps along the length of the magnet (represented by the flat profiles of the field along the y-axis in the middle

A. An array of single magnets



B. Magnetic field on plane a



C. Magnetic field on plane b in the gap_T

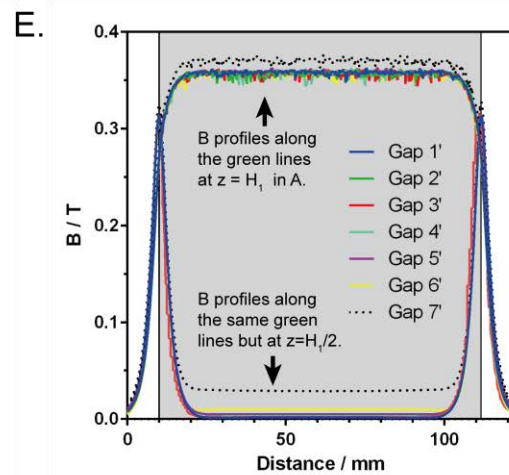
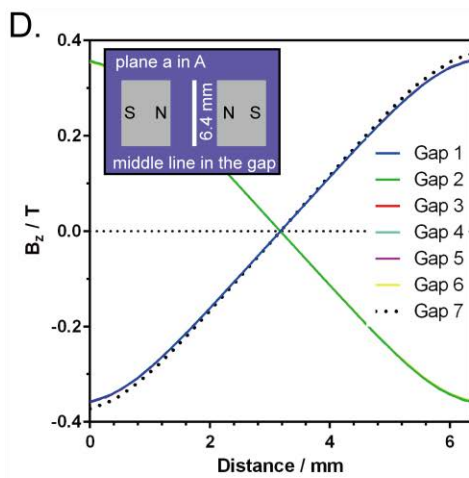
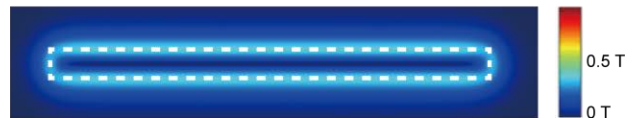


Figure S1 Selection of the number and dimensions of the magnets to create an identical profile of magnetic field for all the tubes on a 96-well plate. (A) A schematic of the spatial arrangement of the magnets. In this schematic, we showed only half of the array (only the top magnets) that we constructed experimentally. Plane a on the x-z plane cuts through the magnet array at half its length ($L/2$ along y-axis). Plane b on the y-z plane sits in the middle of the 1' gap. The red lines represent the vertical symmetric axes of the gaps. The green lines run along the y-axis in the middle of the gaps, and (as shown) are on the same plane as the top faces of the magnets. (B) The profile of magnetic field strength (represented by the absolute magnitude of the field, $\|B\|$) on plane a. (C) The profile of magnetic field strength ($\|B\|$) on plane b. The dashed box indicates the magnets in the y-z plane. (D) B_z along the white lines in (A). (E) $\|B\|$ along the green lines in (A) at two heights of $z=H_1$ (as shown in (A)) and $z=H_1/2$. The grayed region represents the length ($L=4''$ or ~ 101.6 mm) of the magnets.

segments, Figure S1E). The magnetic field is not uniform—as expected—towards the edge of the magnets. The uniform profile of the field is important to ensure that all eight tubes in a single column on the plate (which spans ~63 mm) experience indistinguishable magnetic fields.

Third, we optimized the specific dimensions of the magnets—the width (W) and height (H_1). Eq 2 in the main text suggests that for a given concentration of paramagnetic medium (and thus a fixed value of the magnetic susceptibility of the suspending medium), the measurable range of density is determined by the characteristics of the magnetic field as indicated by the $B_z(dB_z/dz)$ term; we, therefore, evaluated its dependence on the dimensions of the magnets.

In the simulation, we placed the origin of the z -axis at the bottom of the tube to maximize the use of the space between the magnets for density measurements. We then set the bottom faces of the magnets at $z=0$ and swept the height of the magnets H_1 —and the width of the magnets changes accordingly as the magnets adapt to the tubes on the plate. We quantitatively evaluated the influence of height of the magnets on the z -component of the field B_z and the term $B_z(dB_z/dz)$.

Figure S2B and S2C show that as the height of the magnets increases from 2 mm to 12 mm, the z -component of the magnetic field B_z increases to reach a maximum at $H_1 \sim 6$ mm while $B_z(dB_z/dz)$ reaches its maximum earlier at $H_1 \sim 4$ mm. As H_1 increases beyond ~8 mm, neither B_z nor $B_z(dB_z/dz)$ is linear. Given the commercial availability of magnets (Long and thin NdFeB magnets are brittle and susceptible to mechanical breakage, and are only available in limited selection of sizes and shapes even for customized magnets), and the physical dimensions of the 96-well plate, we used 15

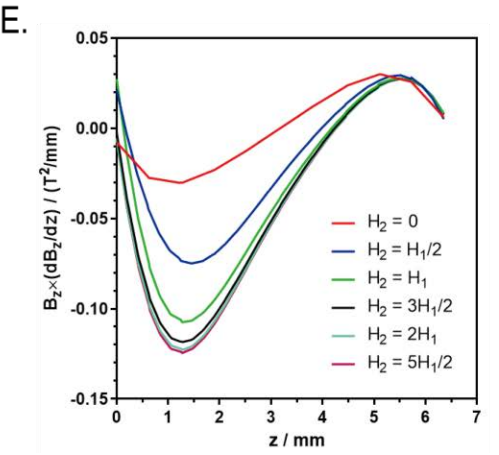
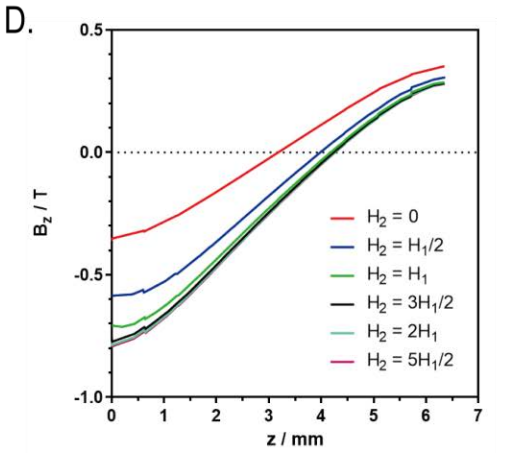
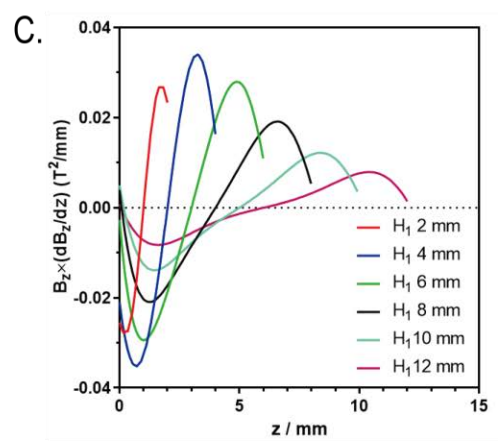
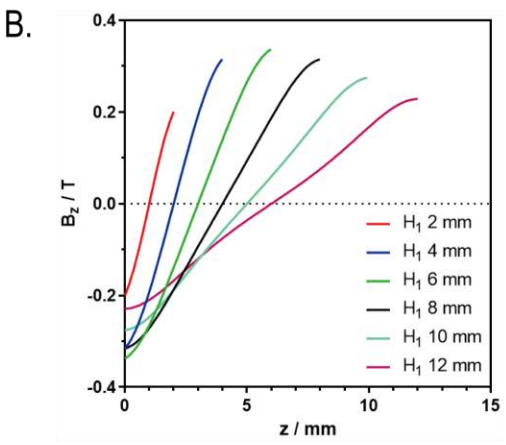
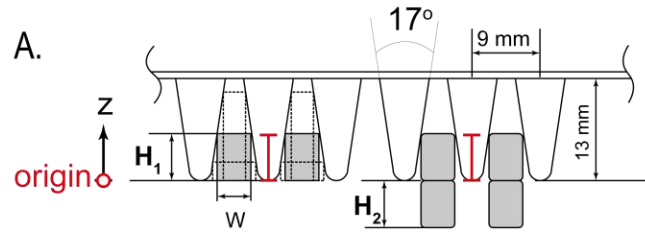


Figure S2 Simulation-guided selection of the dimensions of the magnets (A) A schematic of the spatial arrangement of the magnets and the tubes on a 96-well plate that we used for the simulation. In the simulation, we set the origin of the z-axis at the bottom of the tube, and then fix the bottom face of the (top) magnet at $z=0$, while allowing the height and width of the magnet to change according to the contour of the external surface of the tube. (B) and (C). B_z and the derived term $B_z \times (dB_z/dz)$ along the central line (the red line on the left in A) as the height of the magnets (H_1) varies. (D) and (E) B_z and the derived term $B_z \times (dB_z/dz)$ along the central line (the red line on the right in A) as the height of the bottom magnets (H_2) varies while maintaining $H_1=6.4$ mm.

magnets of $H_1=6.4$ mm to generate uniform magnetic fields for all of the tubes on a plate, while maximizing both the working distance and the gradient of the magnetic fields.

Lastly, we stacked a second a second set of magnets at the bottom of the first set to increase the strength of the magnetic field further, and thus, to reduce the concentration of the paramagnetic species in the medium required to levitate samples. We exploited the strong magnetic field around the boundary where two opposite poles of the magnets meet as shown in Figure 2C in the main text. In the simulation, we used the same width and length for the second set of magnets, and swept its height H_2 . The B_z at $z=0$ in the gap (Figure S2D) clearly increases when the height of the second set of magnets H_2 increases from zero to $H_2 = H_1$, and then quickly plateaus beyond $H_2 > H_1$. We, therefore, simply selected $H_2 = H_1$ for the final configuration we describe in this study. We estimated that this simple approach of stacking magnets increased $B_z(dB_z/dz)$ by $\sim 4\times$ (at $z=1.5$ mm, Figure S2E)—that is equivalently we may use $\sim 4\times$ diluted paramagnetic medium to levitate samples of the same density (eq 2 in the main text).

Design an apparatus to image samples that levitate in a 96-well plate using a scanner

We used a flatbed scanner to acquire images of the levitated samples in a 96-well plate, and designed an apparatus (including a flatbed scanner and a simple interface) using mirrors and relay lenses to project focused images of the levitated samples to the scanner bed. Figure S3 shows the design of the apparatus we implemented in this study, and Table S1 lists the dimensions for the spatial arrangement of the key components. Logistically, we first used simple models (based on ray diagrams) to guide the selection of specific sets of parameters for the key components (e.g. angles of mirrors,

Table S1 Spatial arrangement of mirrors and lenses

Tube No.	1	2	3	4	5	6	7	8
Lateral shift of the mirror (D , mm)	-24.0	-15.0	-6.0	3.0	12.0	21.0	30.0	39.0
Angle of the mirror	40.2°	42.0°	43.8°	45.6°	47.4°	49.2°	51.0°	52.8°
Lateral shift of the lens (x_p , mm)	-23.4	-15.0	-6.5	1.8	10.2	18.5	27.2	35.6

*note: See Figure S3 for assignment of Tube No. All values are reported with respect to the central axis of the scanner, and the direction of the lateral shift of the illumination is designated as “positive”.

and lateral shifts of relay lens with respect to the tubes), and then optimized these dimensions empirically to arrive at the final values. We describe the specific configurations for the three key parts (the scanner, the mirrors, and the lens) of the apparatus in detail.

(1) The scanner

We used the scanner (Epson®, Perfection, V600), and its associated software (specifically, the “film” mode) to control and acquire the images. The scanner has a flatbed with a width 223 mm, and, in its closable lid, a LED that provides a uniform, line illumination (83 mm). The lid is physically attached to the body of the scanner (through a cable), but can be raised from the body of the scanner for a maximum distance of ~65 mm—a distance large enough to accommodate the MagLev device. The LED traverses, during scanning, along the central axis of the scanner, and illuminates a strip that overlaps the central axis of the scanner with a lateral shift of ~7.5 mm in the orthogonal direction to the central axis. The scanner and the software records the central region of the strip with a width of ~60 mm.

When the scanner is used to image 3D-objects (e.g. the MagLev device), it provides an oblique view, that is objects placed further away from the central axis of the scanner appear to be tilted toward the axis (Figure S4B). This observation probably originates from the optics of the scanner, and is not a surprise given the fact that the scanner is usually optimized to image thin, 2D sheets. We used a simple convex lens to model the optics internal to the scanner (which we presume is based on a similar design), and estimated the critical parameter (~240 mm, based on the simple model as we described in Figure S4), the distance of physical separation between the flatbed and the

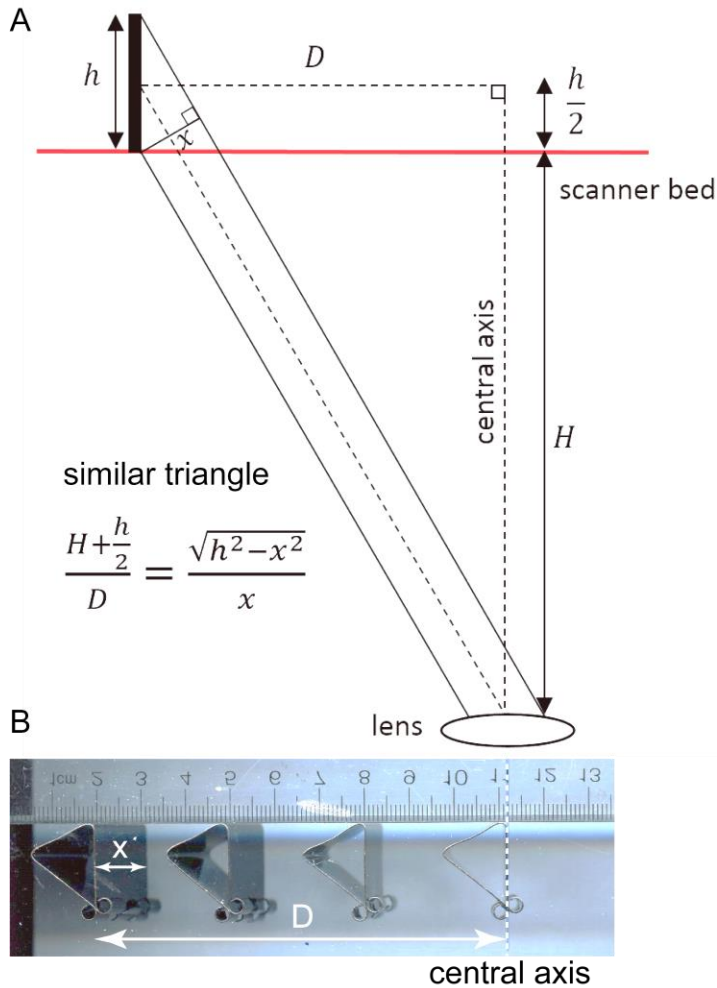


Figure S4. Estimation of the physical separation of the lens and flatbed of the scanner (A) a schematic of a simple optical system to model the optics internal to the scanner. An object with a height of h is placed on the flatbed at a distance of D to the central axis of the scanner, and has a perceived length of x in the image acquired by the scanner. We used similar triangle to calculate the physical separation, h , of the flatbed and the lens. (B) Four binder clips ($h=32$ mm), along with a ruler, were placed on the scanner at various distances (marks on the ruler: 2.0 cm, 5.0 cm, 8.0 cm and 11.2 cm) to the central axis (dashed white line).

lens of the scanner. We used this parameter to design and guide the spatial placement of mirrors and lenses.

(2) The mirrors

All mirrors were inserted in the gaps of the magnet array of at $\sim 45^\circ$ facing downward to project images of the individual tubes. In each of the 12 gaps, we inserted a total of eight mirrors at an inter-mirror separation of 9 mm, positioned the centers of the mirrors at the half height of the top magnets, and finally aligned the row of mirrors symmetrically about the axis of illumination. Because of the axis of illumination is laterally shifted by +7.5 mm (we defined the shifts in the direction of the illumination axis as positive values), the coordinates for the centers of the mirrors are thus the following: 39, 30, 21, 12, 3, -6, -15, -24 (mm).

We finely tuned the angles of the mirrors for tubes situated at different distances to the central axis of the scanner to provide a non-oblique view of the sample that levitate in these tubes. Because of the shape of the magnetic field, the samples, e.g., small particles, form horizontal lines within the tubes. We adjusted the spatial arrangements of the mirrors and lenses such that the lines appeared as single dots on the acquired images.

We developed a simple model (Figure S5) to estimate the angle at which the axis of the tube in the reflected image is perpendicular to the line defined by the centers of the mirror and the lens of the scanner, and used this angle to provide an non-oblique view of the samples in the tube.

(3) The lens

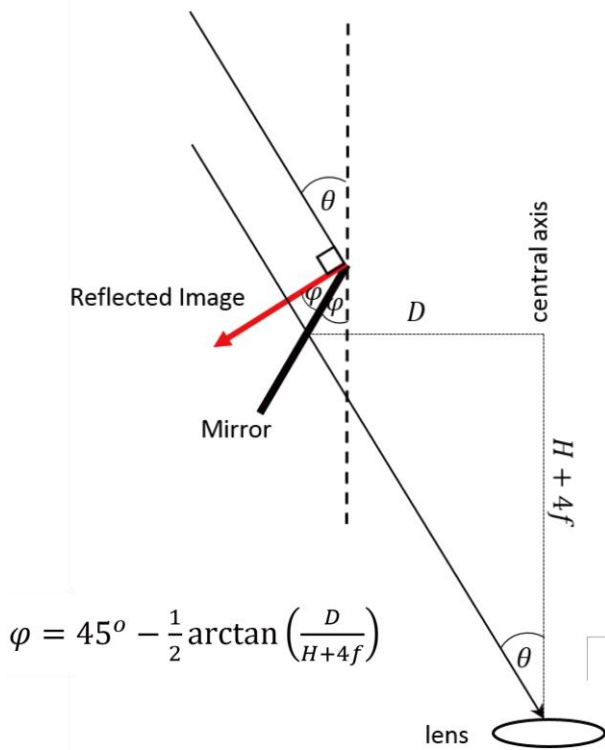


Figure S5. Determination of the optimal angles of the mirrors to provide a “head-on” view of levitating objects. The center of the mirror is positioned at $4f$ above the flatbed of the scanner. f is the focal length of the relay lens, and H is the distance between the flatbed and the lens of the scanner. A relay lens (not shown), when placed at a distance of $2f$ below the tube, will project an image of the tube to the flatbed of the scanner at a distance of $2f$ with a 1:1 magnification. D is the distance of the mirror to the central axis.

We placed relay lenses below the mirrors to project images of the tubes to the flatbed of the scanner. We shifted the lenses toward the central axis of the scanner such that the central portion of the tubes became visible to the scanner. We used the following model (Figure S6) to estimate the lateral shifts of the lenses with respect to the central axis, and used these estimates (for a total of eight lenses for a single column of tubes on the plate) as the initial set of values to optimize the lateral shifts of the lenses.

Assembly of the device

We used 3D-printed plastic parts to house the magnets and assemble the supporting components (e.g. mirrors and lenses). Figure S7 depicts the major components in the fully assembled device.

Analysis of Images

We processed images of each well with custom software to determine the positions of the levitated samples relative to the center of the viewing circle. We calibrated each well based on the measured locations of density standards (~200 μm colored particles). We then measured the densities of samples not used during calibration and compared our experimentally-measured densities with literature values. The software identified and segmented samples based on either a distinguishing color or a change in contrast at the boundary of the samples.

We identified the center of each viewing circle by converting an image of the well to binary with a threshold value of 0.047 using the `im2bw()` function in Matlab and computing the centroid of the largest connected region.

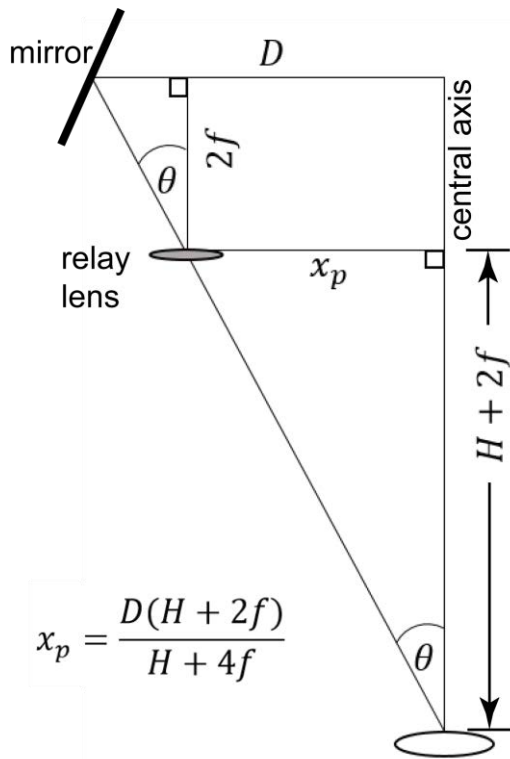


Figure S6. Estimation of the lateral shifts of the lenses, x_p , with respect to the central axis of the scanner. f is the focal length of the relay lens.

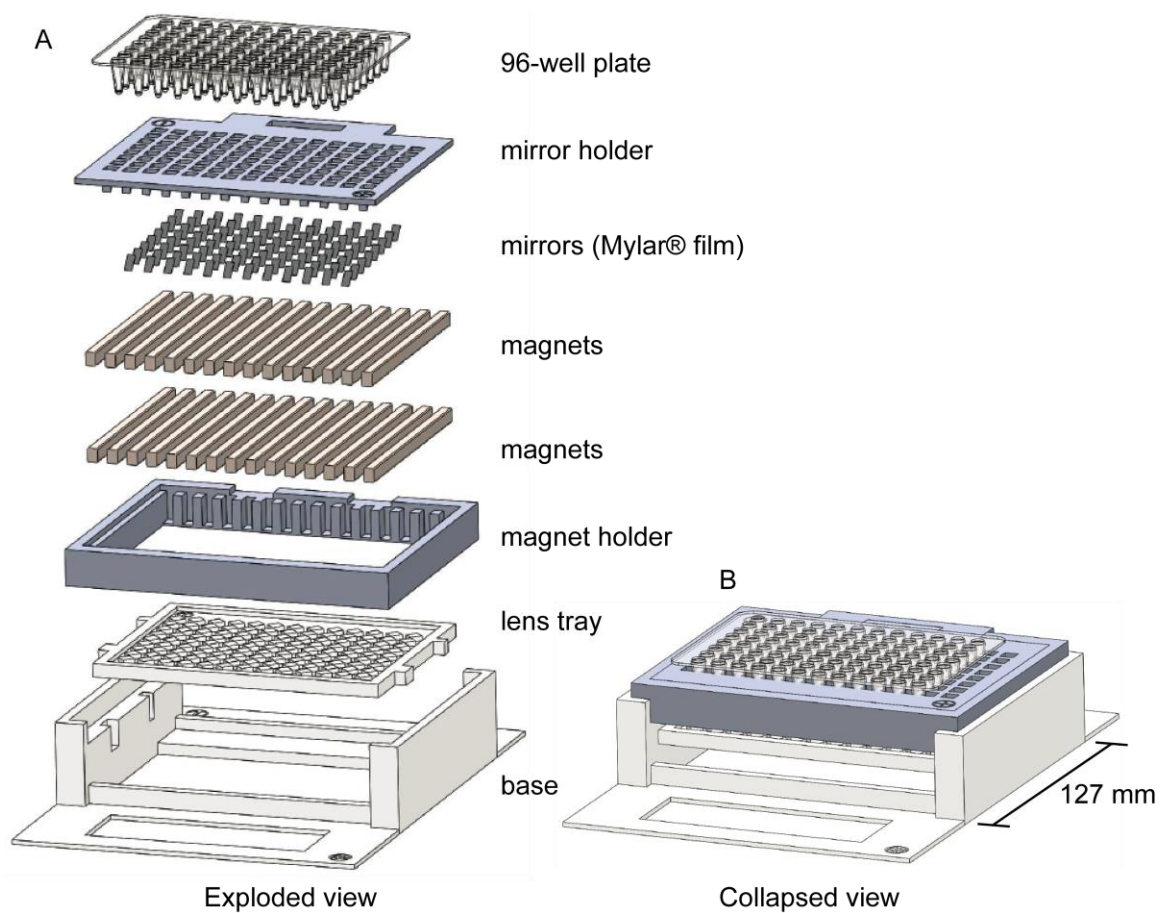


Figure S7. Exploded and collapsed views of the final assembled device.

We identified samples with colors clearly distinguishable from the background primarily based on their hue value. This was the case for all four of the density standards that we used for calibration (Figure S8). Occasionally, the background may also show a faint color similar to the particles (it was caused by both the fluorescence that these dyed particles emitted under the conditions we carried out the experiment, and the natural color of the plastic housing we used.); the color, however, did not interfere with the determination of the positions of these particles. Cut-off hue values and other specifications are detailed in Table S2.

Several of the samples that we measured experimentally lacked a distinguishing color; we were not able to identify the locations of these samples using the procedures as described above. Instead, we used edge detection to determine the location of these samples (Figure S9).

We analyzed the spread in density of samples of red blood cells by fitting a normal distribution to the density distribution of the cells (Figure S10). The density distribution was measured experimentally by comparing with an in-situ calibration performed by fitting the measured locations of density standards (the green and blue particles).

We described the preceding image processing and analysis operations on a per-well basis. To evaluate the entire 96-well plate, we ran these operations in a loop over an image of the entire plate, where the image of the entire plate was spliced into 96 sections (8×12), each of which was analyzed serially.

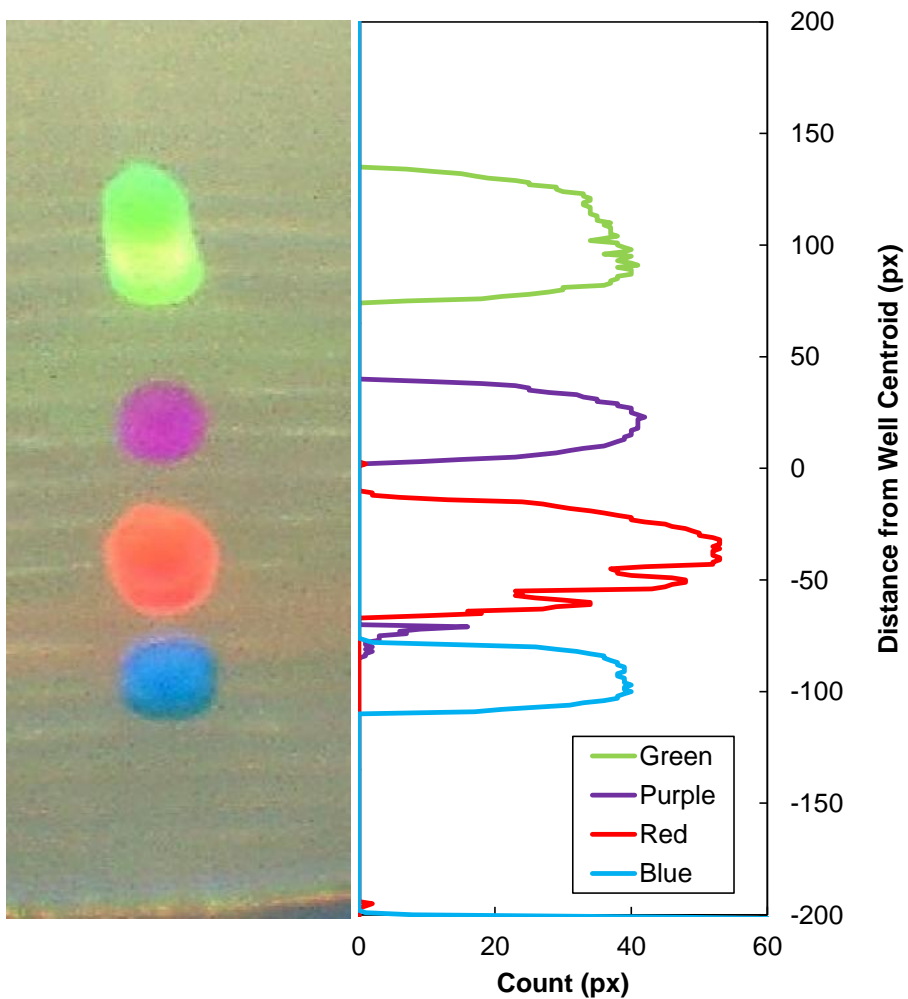


Figure S8. Image processing of colored particles in a well to determine their locations relative to the well centroid.

Table S2. Identifiers and constraints used to segment colored particles from images.

Color	Identifier 1	Constraint on 1	Identifier 2	Constraint on 2
Green	Hue	$0.17 < H < 0.45$	Value	$H > 0.97$
Purple	Hue	$0.80 < H < 0.98$	Value	$H > 0.60$
Red	Hue	$0.01 < H < 0.07$	Value	$H > 0.75$
Blue	Hue	$0.45 < H < 0.65$	Red Channel	$R < 0.35$

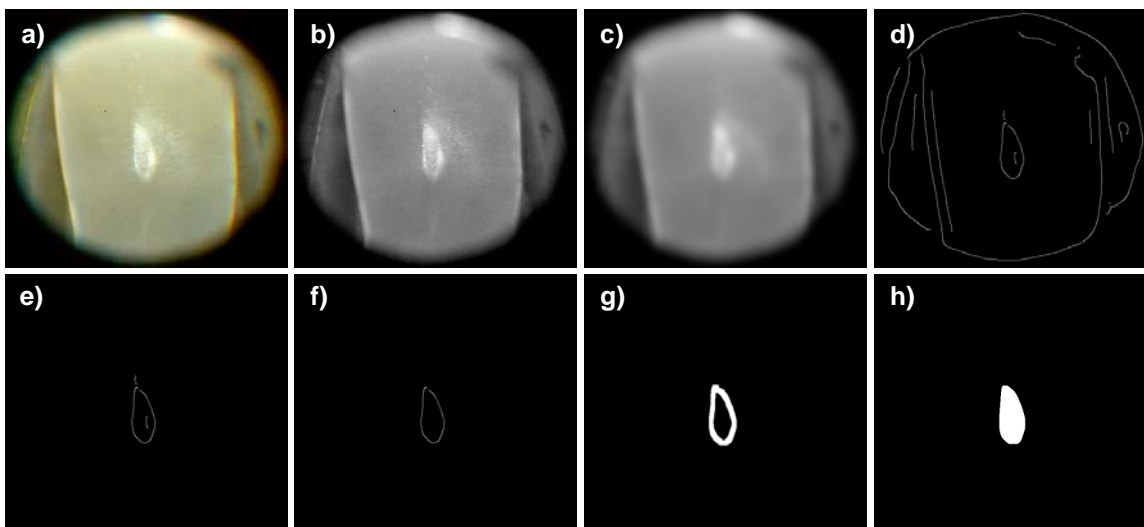


Figure S9. Processing of an image of cholesterol suspended in a well using an edge detection algorithm. Starting from the original image (a), the value channel of the hue-saturation-value representation is extracted (b) and blurred with a Gaussian filter (c). Edges are detected with the Canny edge detection algorithm (d), and regions outside of the well are cropped (e). Finally, artefactual edges under a threshold length are removed (f), the remaining edges are dilated (g), and the region of interest within the edges is filled as a convex hull of the edge pixels.

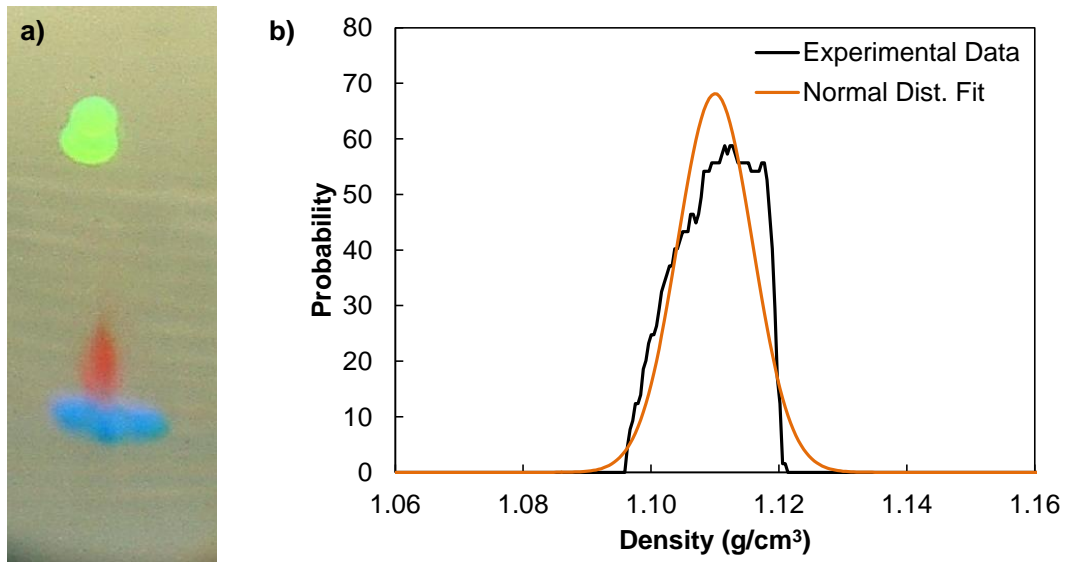


Figure S10. The spread in density for a sample of red blood cells was determined by first calibrating the density in-situ using the density standards (a, the green and blue particles), and then fitting a normal distribution to the density distribution of the cells (b). For this sample, the estimated mean density of the red blood cells was 1.11 g/cm³, and the spread, represented by the standard deviation, was ~ 0.01 g/cm³.

Estimation of the uncertainty of measurements for samples in single tubes using calibration curves

We used a set of four colored particles to calibrate the density measurements in individual wells, and here, estimated the uncertainty in the estimated values of densities of samples using the calibration curves if we treat single tubes as independent measurements.

Eq S1 gives the equation for the best-fit for the plot of density vs. the distance D of the colored particles to the center of the viewing area. We used four pairs of data (D_i, ρ_i) ($i=1-4$) to establish the calibration curve for each tube. For this discussion, D (unitless) simply represents the number of pixels on the image, and is negative when the centroid of the particles are below the center of the viewing area on the image. (We did not convert the number of pixels to physical distances for this example.) ρ (kg/m³) is the average density of the particles.

$$D = m\rho + b \quad (S1)$$

For a sample with unknown density (e.g., a cluster of particles), we first determine its D , and then insert it to eq S1 to calculate its density.

Eq S2 gives the uncertainty, $\delta\rho$, in the estimate of density using the calibration curve, Eq S1.¹ In eq S2, S_D is the standard deviation of the vertical distances on the calibration curve between the D -coordinates of the colored particles and the best-fit curve, $|m|$ is the absolute value of the slope, k is the number of replicate measurements of the unknown sample, n is the number of data points to establish the calibration curve, \bar{D} is the average of the D for the colored particles, $\bar{\rho}$ is the average of the densities for the

colored particles, and D is the distance between the centroid of the sample to the center of the viewing circle.

$$\delta\rho = \frac{S_D}{|m|} \sqrt{\frac{1}{k} + \frac{1}{n} + \frac{(D-\bar{D})^2}{m^2 \sum(\rho_i - \bar{\rho})^2}} \quad (S2)$$

We applied eqs S1 and S2 to estimate the density, and its associated uncertainty, of a sample of 3-chlorotoluene (a single measurement, $k = 1$) in the tube shown in Figure 6A, and obtained $1.068 \pm 0.006 \text{ g/cm}^3$.

Experimental determination of the magnetic susceptibility of a paramagnetic medium

We determined experimentally the magnetic susceptibility of an aqueous solution of nominal 3 M DyCl_3 . We first diluted the concentrated solution by $6\times$ to yield an aqueous solution of nominal 0.5 M DyCl_3 , and then levitated a set of glass beads (1.0200, 1.0630, 1.1100, and 1.1550 g/cm^3) with precisely known densities ($\pm 0.0002 \text{ g/cm}^3$) using the standard MagLev device. We used a ruler with a minimal division of 1 mm (read to $\pm 0.1 \text{ mm}$) to measure the levitation heights of the beads.

We plotted the density vs. h , and performed linear fit, which yielded eq S3:

$$\rho = -6663(\pm 187)h + 1267(\pm 5) \quad (S3)$$

In eq S3, ρ (kg/m^3) is the density of a sample that levitated at a distance of h (m) to the surface of the bottom magnet. The slope is presented as best-fit value \pm standard deviation of the best-fit value.

Eqs S4-6 give the formulas for ρ vs. h using the standard MagLev device.²

$$\rho = \alpha h + \beta \quad (S4)$$

$$\alpha = \frac{(\chi_s - \chi_m)4B_0^2}{g\mu_0 d^2} \quad (S5)$$

$$\beta = \rho_m - \frac{(\chi_s - \chi_m)2B_0^2}{g\mu_0 d^2} \quad (S6)$$

In eqs S5 and S6, χ_s (unitless) is the magnetic susceptibility of the sample, χ_m (unitless) is the magnetic susceptibility of the paramagnetic medium, B_0 (T) is the maximum strength of the linear magnetic field along central axis in the gap between the two facing magnets, g (9.8 m/s²) is the constant of gravitational acceleration, μ_0 ($4\pi \times 10^{-7}$ N•A⁻²) is the magnetic permeability of the free space, d (m) is the distance of separation of the two magnets, ρ_m (kg/m³) is the density of the paramagnetic medium.

We used eqs S3 and S5 to calculate the magnetic susceptibility of the solution, χ_m , and the part that contributed by the DyCl₃, χ'_{DyCl_3} . Eqs S7 and S8 give the rearranged equations for the calculation.

$$\chi_m = \chi_s - \frac{\alpha g \mu_0 d^2}{4B_0^2} \quad (S7)$$

$$\chi'_{DyCl_3} = \chi_m - \chi_{H_2O} \quad (S8)$$

To calculate the χ'_{DyCl_3} , we used the experimentally measured values for B_0 (0.385 T), and d (45.0 mm). We estimated the magnetic susceptibility of the glass bead, χ_s , using a simple model in which the glass beads (we used $\rho_{bead} = 1.1100$ g/cm³ for this calculation) consist of glass ($\rho_{glass} \approx 2.4$ g/cm³, $\chi_{glass} = -1.39 \times 10^{-5}$), and an air pocket (we assumed zero density or magnetic susceptibility).³

$$\chi_{bead} = \chi_{glass} \left(\frac{V_{glass}}{V_{bead}} \right) = \chi_{glass} \left(\frac{\rho_{glass}}{\rho_{bead}} \right) = -3.0 \times 10^{-5} \quad (S9)$$

In eq S8, χ_{H_2O} is the magnetic susceptibility of water (-9.0×10^{-6}).

We assumed that the major uncertainty in estimating the χ_{DyCl_3} stemmed from the uncertainty of the linear fit, and estimated the magnetic susceptibility of the diluted DyCl₃ solution, χ'_{DyCl_3} :

$$\chi'_{DyCl_3} = (2.60 \pm 0.08) \times 10^{-4} \quad (S10)$$

We, therefore, determined the magnetic susceptibility of the original solution of nominal 3 M DyCl₃:

$$\chi_{DyCl_3} = (2.60 \pm 0.08) \times 10^{-4} \times 6 - 9.0 \times 10^{-6} = (1.56 \pm 0.05) \times 10^{-3} \quad (S11)$$

Calculation of the density of a cluster of particles

We first estimated the magnitude of the $B_z(dB_z/dz)$ at distance D (with respect to the center of the viewing circle, Figure 6A) using the calibration curves established by the small, colored particles.

Eq S12 gives the equation of the linear fit for the colored particles in a tube.

$$D = m\rho + b \quad (S12)$$

Eq S13 is the same equation, eq 2, that we described in the main text. This equation allows us to estimate the value of $B_z(dB_z/dz)$ at the position a sample levitates (e.g., density particles having a known density and a magnetic susceptibility) in a paramagnetic medium with a known density and a magnetic susceptibility.

$$\rho = \frac{(\chi_s - \chi_m)}{\mu_0 g} \left(B_z \frac{dB_z}{dz} \right) + \rho_m \quad (S13)$$

We combined eqs S12 and S13 to give eqs S14-17 that we can use to estimate the value of $B_z(dB_z/dz)$ at any distance D in the linear range we characterized using the colored particles.

$$B_z \frac{\partial B_z}{\partial z} = \frac{\mu_o g}{m(\chi_s - \chi_m)} D - \frac{\mu_o g(b/m + \rho_m)}{(\chi_s - \chi_m)} \quad (S14)$$

$$K_1 = \frac{\mu_o g}{m(\chi_s - \chi_m)} \quad (S15)$$

$$K_2 = \frac{\mu_o g(b/m + \rho_m)}{(\chi_s - \chi_m)} \quad (S16)$$

$$B_z \frac{\partial B_z}{\partial z} = K_1 D - K_2 \quad (S17)$$

We calculated the values of K_1 and K_2 for each tube using the calibration curve that we constructed using the set of four, colored particles (1.03, 1.06, 1.10, 1.13 g/cm³). In this experiment, we used an aqueous solution of 0.100 M MnCl₂ (We prepared this solution from a stock solution, 3.000±0.001 M) to levitate the particles, and calculated its density and magnetic susceptibility using the formula as we described elsewhere in detail:²

$$\rho_m = 1008.1 \text{ kg/m}^3$$

$$\chi_m = 9.58 \times 10^{-6}$$

The small density particles we used are based on polyethylene, and they have a magnetic susceptibility χ_s of -9.50×10^{-6} .⁴

We estimated K_1 and K_2 for each individual tube. We combined individual values of K_1 or K_2 across the plate, and obtained the averages for $K_1 = 0.28 \pm 0.03$ (mean±SD, T²/m), and $K_2 = 31 \pm 14$ (mean±SD, T²/m).

We next determined the centroid of a cluster of the copper or glass particles that levitated in an aqueous solution of 3 M DyCl₃, and used eq S17 (and its associated pair of K_1 and K_2) to estimate the value of $B_z(dB_z/dz)$ at that distance D .

We finally inserted the estimated value of $B_z(dB_z/dz)$, the experimentally measured density of the DyCl_3 solution (1.6927 g/cm^3), and the estimated magnetic susceptibility of the DyCl_3 solution (1.56×10^{-3} , eq S11), to calculate the density of the cluster of the copper or glass particles. In this calculation, we neglected the magnetic susceptibility of the sample (i.e., the copper and glass particles) because they are negligible compared to the magnetic susceptibility (1.56×10^{-3}) of the DyCl_3 solution that we used to levitate the samples.

We obtained the averages of the estimated densities across the plate for the sample of copper powder ($7.7 \pm 0.6 \text{ g/cm}^3$, $N=95$ wells) and for the sample of glass particles ($2.4 \pm 0.4 \text{ g/cm}^3$, $N=95$ wells).

References

- (1) Harris, D. C. *Quantitative Chemical Analysis*; 7th ed.; W. H. Freeman and Company, 2007.
- (2) Mirica, K. A.; Shevkoplyas, S. S.; Phillips, S. T.; Gupta, M.; Whitesides, G. M. *J Am Chem Soc* **2009**, *131*, 10049-10058.
- (3) Nemiroski, A.; Soh, S.; Kwok, S. W.; Yu, H. D.; Whitesides, G. M. *J Am Chem Soc* **2016**, *138*, 1252-1257.
- (4) Calleja, F. J. B. *Journal of Polymer Science Part C: Polymer Symposia* **1967**, *16*, 4311-4321.